JGR Space Physics

RESEARCH ARTICLE
10.1029/2019JA026698

Key Points:

- SAPS is investigated with the Coupled Magnetosphere-Ionosphere-Thermosphere model with ring current extension
- SAPS global structures are characterized with the model and shown to be consistent with observations
- SAPS dynamic evolution and its dependence on the IMF B_Z are quantitatively analyzed

Correspondence to:
D. Lin,
ldong7@vt.edu

Citation:
Lin, D., Wang, W., Scales, W. A., Pham, K., Liu, J., Zhang, B., et al. (2019). SAPS in the 17 March 2013 storm event: Initial results from the coupled magnetosphere-ionosphere-thermosphere model. *Journal of Geophysical Research: Space Physics*, *124*, 6212–6225. https://doi.org/10.1029/2019JA026698

Received 6 MAR 2019
Accepted 11 JUN 2019
Accepted article online 2 JUL 2019
Published online 22 JUL 2019

©2019. American Geophysical Union.
All Rights Reserved.

SAPS in the 17 March 2013 Storm Event: Initial Results From the Coupled Magnetosphere-Ionosphere-Thermosphere Model

Dong Lin[1,2], Wenbin Wang[2], Wayne A. Scales[1], Kevin Pham[2], Jing Liu[2], Binzheng Zhang[2], Viacheslav Merkin[3], Xueling Shi[1], Bharat Kunduri[1], and Maimaitirebike Maimaiti[1]

[1]The Bradley Department of Electrical and Computer Engineering, Virginia Tech, Blacksburg, VA, USA, [2]High Altitude Observatory, National Center for Atmospheric Research, Boulder, CO, USA, [3]The Applied Physics Laboratory, Johns Hopkins University, Laurel, MD, USA

Abstract Subauroral polarization stream (SAPS) is latitudinally narrow flow channels of large westward plasma drifts in the subauroral ionosphere. In this study, the global structure and dynamic evolution of SAPS are investigated by using the Coupled Magnetosphere-Ionosphere-Thermosphere model with ring current extension, namely, the Lyon-Fedder-Mobarry-Thermosphere Ionosphere Electrodynamics General Circulation Model-Rice Convection Model, to simulate the 2013 St. Patrick's Day storm event. This is the first time that the global distribution and temporal evolution of SAPS are investigated using first-principle models. The model shows a strong westward ion drift channel formed equatorward of the auroral electron precipitation boundary on the duskside, which is identified as the SAPS structure. The simulated ion drift velocity and auroral electron precipitation sampled along the trajectory of the Defense Meteorological Satellite Program F18 satellite are in good agreement with the satellite measurements. SAPS initiate in the predusk sector when the interplanetary magnetic field turns southward. SAPS latitude generally decreases with magnetic local time from dusk to midnight. The SAPS channel shows wedge, inverse wedge, and crescent morphologies during the storm and becomes discontinuous when the interplanetary magnetic field is weakly southward. The SAPS mean latitude has a correlation coefficient of 0.77 with the Dst index. The mean latitude moves equatorward, and the flow channel broadens in the storm main phase. The simulation results illustrate both the global distribution and highly dynamic behavior of SAPS that are not readily apparent from the observation data.

1. Introduction

The ionospheric subauroral convection is frequently characterized by enhanced westward flows driven by strong poleward electric field during geomagnetically active times. The flow channel spans from the duskside to postmidnight and has latitudinal width of a few degrees. The peak magnitude of the drift velocity ranges from a few hundred meters per second to a few kilometers per second. Historically, the localized (1–2° latitudinal width) and intense (>1 km/s) flow channels near the midnight have been termed as polarization jets or subauroral ion drifts (Galperin et al., 1974; Spiro et al., 1979). Broader regions of westward plasma drift equatorward of auroral electron precipitation have also been reported (e.g., Foster & Vo, 2002; Yeh et al., 1991). Foster and Burke (2002) suggested an inclusive name for these subauroral flows: subauroral polarization streams (SAPSs).

The average characteristics of SAPS have been described in statistical studies. Foster and Vo (2002) surveyed 22 years of data from the Millstone Hill incoherent scatter radar and found that SAPSs are persistent from dusk to the early morning sector for all Kp greater than four conditions. It was also found that the peak velocity is on average >900 m/s premidnight and 400 m/s in the predawn sector. The latitudinal width is generally 3° to 5°. Another statistical study based on the Super Dual Auroral Radar Network radars shows that SAPS can be observed 15% of the time during relatively quiet conditions (-10 nT < Dst < 10 nT), and 87% of the time during moderately disturbed conditions (-75 nT < Dst < -50 nT; Kunduri et al., 2017). During the quiet times, SAPSs are found to be localized to the midnight and centered above 60° magnetic latitude. During moderately disturbed conditions, SAPSs are found to be centered at 20 magnetic local time

(MLT) and below 60° magnetic latitude. The SAPS velocities are found to increase nearly linearly with MLT during low and moderate geomagnetic activities. SAPS have also been studied with satellite data such as the Defense Meteorological Satellite Program. He et al. (2017) analyzed the different evolution patterns of SAPS during intense storms and quiet time substorms with DMSP data. They found that SAPSs usually occur 0–3 hr after the beginning of the storm main phase and 0–2 hr after the substorm expansion onsets. While the statistical studies can provide the average picture of SAPS under different external driving conditions, it has been a challenge so far to fully describe the global structure of SAPS and how they evolve in a dynamic manner during particular events.

SAPSs have been found intimately connected to the multiway coupling among the solar wind, magnetosphere, and ionosphere-thermosphere. The generation and evolution of SAPS are closely related to the southward IMF (He et al., 2017). Observations have shown that SAPS/subauroral ion drifts are coincident with the region 2 field-aligned current (FAC) flowing into the ionosphere and ion precipitation (e.g., Anderson et al., 2001; He et al., 2014; 2016; Yuan et al., 2016, 2017). When mapping along the magnetic field line to the magnetospheric equatorial plane, SAPS peak locations have been shown to correspond to the inner edge of the ion plasma sheet and are close to the peak of the ring current (Huang & Foster, 2007). SAPS flow variations are often connected to earthward plasma sheet flow bursts and the plasma pressure distribution in the ring current (e.g., Clausen et al., 2012; Ebihara et al., 2009; Gallardo-Lacourt et al., 2017; Lyons et al., 2015). The development of SAPS is suggested to be associated with the injection of plasma sheet ions/electrons, which establishes the polarization electric fields (e.g., Califf et al., 2016; Garner et al., 2004; Lejosne et al., 2018; Makarevich & Dyson, 2008; Mishin et al., 2017; Yuan et al., 2017). It is also demonstrated that the SAPS electric field can erode the outer plasmasphere, which also correlates with the generation of storm enhanced density and plumes of elevated ionospheric total electron content (TEC) on the dayside (e.g., Foster et al., 2002, 2007; 2014; Foster & Rideout, 2005). SAPS channels are found to be located in a region of low TEC values, which implies low ionospheric conductivity (e.g., Clausen et al., 2012; He et al., 2018; Shinbori et al., 2018). Due to the complex multiway coupling between the magnetosphere and ionosphere-thermosphere, it is necessary to evaluate the magnetosphere and ionosphere-thermosphere as a coupled system in order to have a comprehensive understanding of SAPS.

Computational models have been widely used to explore the effects and driving mechanisms of SAPS. Goldstein et al. (2005) developed a magnetospheric model of SAPS parameterized by the Kp index, which was limited in that it could only capture the gross spatial and temporal characteristics of SAPS. Zheng et al. (2008) adopted an empirical ring current model to simulate SAPS and found that the ionospheric conductance trough is critical to the generation of large magnitude SAPS. Wang et al. (2012) incorporated an empirical SAPS model into the Thermosphere Ionosphere Electrodynamics General Circulation Model (TIEGCM) and investigated the SAPS effects on the global ionosphere and thermosphere during a moderately geomagnetically active period. They found that SAPS can cause an increase in global thermospheric temperature and changes in thermospheric composition. Although the empirically driven models can help us understand specific aspects of SAPS, they are inadequate to describe the dynamic evolution of SAPS under different geophysical conditions.

In recent years, global geospace models and coupled frameworks have been used to explore the generation of SAPS. Yu et al. (2015) used the Block-Adaptive Tree Solar-wind Roe Upwind Scheme global magnetohydrodynamic (MHD) model coupled with the inner magnetospheric ring current model Ring current Atmosphere interactions Model with Self Consistent magnetic field to simulate the 17 March 2013 storm event. The SAPS velocities were underestimated, and its location was more equatorward than that in actual observations. Raeder et al. (2016) used the Open Geospace General Circulation Model, Coupled Thermosphere Ionosphere Model, and Rice Convection Model (RCM) to model the same event. The more consistent locations and velocity with observations are attributed to the inclusion of a self-consistent ionosphere/thermosphere model. Wiltberger et al. (2017) made use of the Lyon-Fedder-Mobarry (LFM) global MHD model coupled with RCM ring current model to simulate the same event. They found that the fast westward plasma flow in the subauroral region is mainly driven by the closure of region 2 FAC, which results from the buildup of large inner magnetosphere pressure gradient and partial ring current during the storm time. The inclusion of anomalous electron heating effects in the ionospheric conductance model could sometimes yield SAPS drift velocities that are more consistent with the observations. Therefore, it is further suggested that the inclusion of an ionosphere-thermosphere model with feedback effects from ionospheric plasma chemical processes and thermospheric neutral dynamics is needed to establish a system-level understanding of SAPS.

Due to the intimately coupled nature of the magnetosphere, ionosphere, and thermosphere, it is critical to self-consistently simulate the dynamical processes from solar wind-magnetosphere interaction to the upper atmosphere when modeling the generation and evolution of SAPS. In this paper, we report the initial results from the Coupled Magnetosphere-Ionosphere-Thermosphere (CMIT) model with ring current extension, namely, the LFM-TIEGCM-RCM (LTR) model framework. This integrated model provides a first-principle representation of the solar wind, magnetosphere, ring current, ionosphere, and thermosphere coupling. SAPS generation, global structure, and dynamic evolution, which typically cannot be obtained from observations and statistical studies, are explored by simulating the 17 March 2013 great storm. This paper is organized as follows: Section 2 introduces the LTR model and gives an overview of the solar wind driving conditions and system-level geospace responses during the storm event. Section 3 presents the analysis of the simulation results, including the identification of SAPS with the simulation results and comparison with the observational data, quantitative characterization of SAPS global structure and dynamic evolution. Section 4 discusses the implications of the model outputs and summarizes the findings of this simulation study.

2. Simulation Setup

2.1. LFM-TIEGCM-RCM

The LTR model is used in this study to investigate the geomagnetic storm that occurred on 17 March 2013. The integrated framework couples the LFM global MHD magnetosphere model (Lyon et al., 2004), the TIEGCM global ionosphere/thermosphere model (Roble et al., 1988; Richmond et al., 1992), and the RCM of the ring current (Toffoletto et al., 2003), via the Magnetosphere-Ionosphere Coupler/Solver (MIX) module (Merkin & Lyon, 2010). Historically, the LFM and TIEGCM were first coupled to establish the CMIT model (Wiltberger et al., 2004; Wang et al., 2004). The LFM and RCM were then coupled into the magnetosphere-ionosphere-ring current model (Pembroke et al., 2012). The LFM-TIEGCM-RCM model has been recently developed to incorporate the RCM into the CMIT.

Figure 1 shows the flow chart of the coupling processes between the LFM, TIEGCM, and RCM. The LFM model solves ideal MHD equations for the interactions between the solar wind and the magnetosphere. Magnetic field and plasma information in the inner magnetosphere is passed from LFM to RCM for the calculation of the ring current distribution in RCM. The plasma density and pressure are then passed from RCM to LFM. FACs are calculated at the inner boundary of LFM and mapped down to the MIX module together with the auroral precipitation, which is determined from the plasma density and temperature (Fedder et al., 1995; Wiltberger et al., 2009). The MIX coupler solves the ionospheric potential and passes the auroral precipitation and electrostatic potential to TIEGCM. The ionospheric and thermospheric circulation and electrodynamics are solved in TIEGCM, which returns the updated ionospheric conductance to MIX. More details about the coupling processes can be found in Lyon et al. (2004), Merkin and Lyon (2010), Pembroke et al. (2012), Wang et al. (2004), and Wiltberger et al. (2004, 2017). It should be pointed out that the coupled model incorporates three-way coupling among the magnetosphere, ring current, and ionosphere-thermosphere, which makes it feasible to investigate geospace from the solar wind to the altitude of the thermosphere with real-time and self-consistent downward driving and upward feedback. The connections represented with dashed lines are not yet implemented in this study but will be implemented in the future.

In this study, the LFM model utilizes the quad resolution, that is, $106 \times 96 \times 128$ cells in the radial, meridional, and azimuthal directions, respectively. The MIX coupler is computed on a $1^\circ \times 1^\circ$ magnetic latitude and longitude grid. The TIEGCM utilizes a longitudinal and latitudinal resolution of 1.25°. The RCM utilizes 200 cells in latitude, 100 cells in longitude, 90 energy channels, and a dipole tilt. It should be noted that previous studies used 15 s or even 1 min for data exchange between the LFM and RCM, and 10 s for data exchange between LFM and MIX (Pembroke et al., 2012; Wiltberger et al., 2017). For the strong solar wind driving conditions considered here, we found it necessary to reduce the intervals of data exchange to 5 s between LFM and MIX and 10 s between LFM and RCM in order to avoid numerical instability. The TIEGCM and MIX exchange interval uses the default 10 s.

2.2. Solar Wind Conditions and Systematic Geospace Responses

The 2013 St. Patrick's Day storm is a famous event that has been surveyed with different models and observational data (e.g., Raeder et al., 2016; Wiltberger et al., 2017; Yu et al., 2015; Zhang et al., 2017). The solar

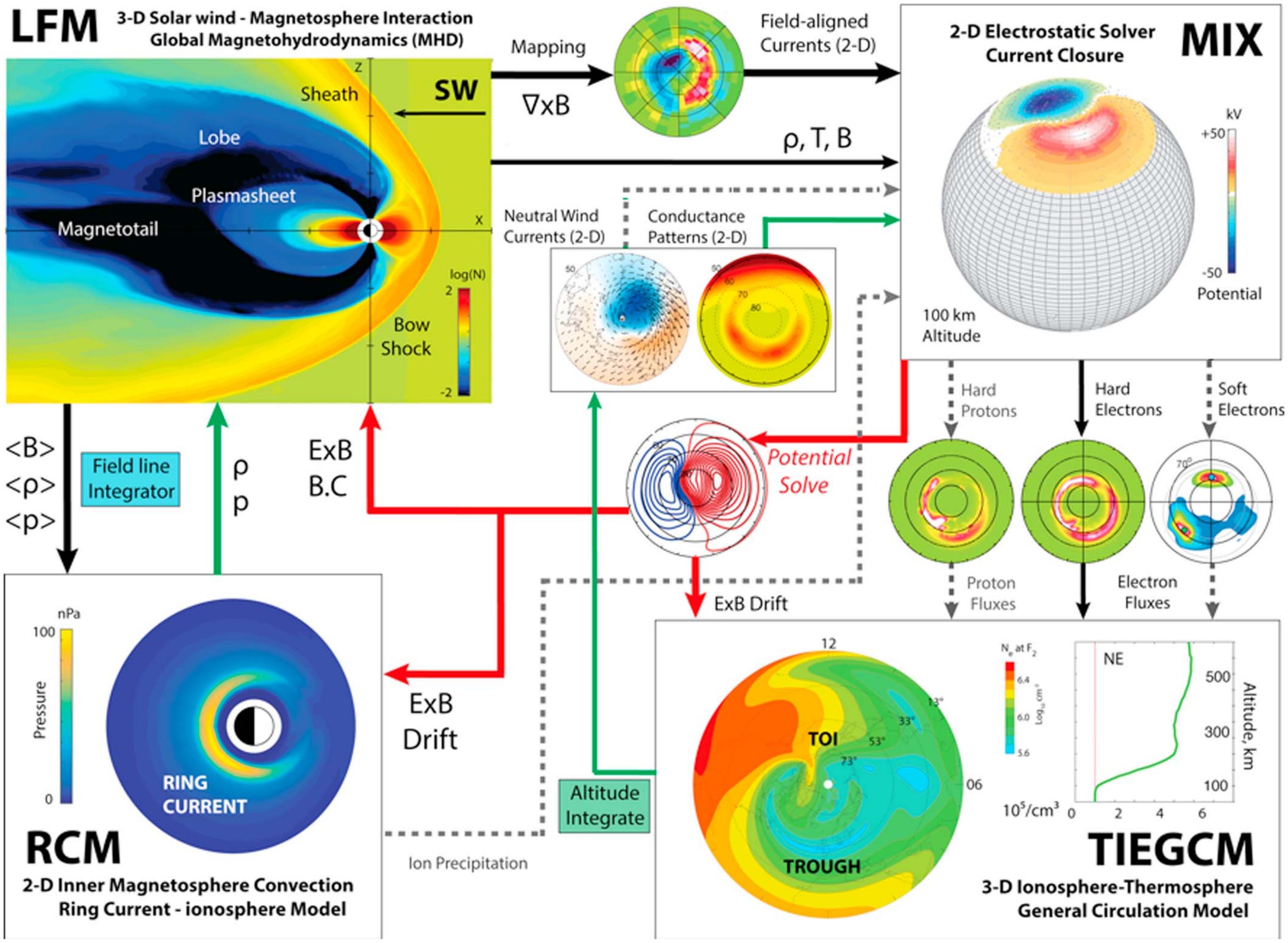

Figure 1. Flow chart of the coupled Lyon-Fedder-Mobarry (LFM)-Thermosphere Ionosphere Electrodynamics General Circulation Model (TIEGCM)-Rice Convection Model (RCM).

wind and IMF conditions for 17 March 2013 are shown in Figures 2a–2d. The data were obtained from the OMNI database and used to drive the LTR model. A coronal mass ejection arrived at the Earth at 05:55 UT and triggered a great geomagnetic storm over the rest of the day. The solar wind density increased to above 10 cm^{-3}, solar wind speed reached −700 km/s, and IMF B_Z reached −20 nT after the coronal mass ejection arrived. The Dst index decreased to below −100 nT in the next 4 to 5 hr and maintained the low level for the rest of that day. The strongly disturbed IMF and solar wind conditions returned to predisturbed conditions by the end of the day.

Figures 2e–2g show the overall geospace response by presenting the time series of the cross polar cap potential and the total FAC in the Northern Hemisphere, and the Dst index. The cross polar cap potential is calculated as the difference between the max and min of the potential (Figure 2e). The total FAC is integrated over the FAC density that flows into the ionosphere (Figure 2f). Here the potential and FAC are both output from the MIX module. The Active Magnetosphere and Planetary Electrodynamics Response Experiment measurements of integrated downward FAC in the Northern Hemisphere are shown with the black curve for comparison. The simulated Dst index is determined from the magnetospheric FACs and the ionospheric horizontal currents by calculating the ground magnetic field perturbations with the Biot-Savart method. The observed Dst index is shown in black and obtained from the CDAWeb OMNI database. The comparison of Dst and total FAC with observational data demonstrates that the LTR model could yield very consistent results of the geospace response to the solar wind driving conditions during the 2013 St Patrick's Day storm.

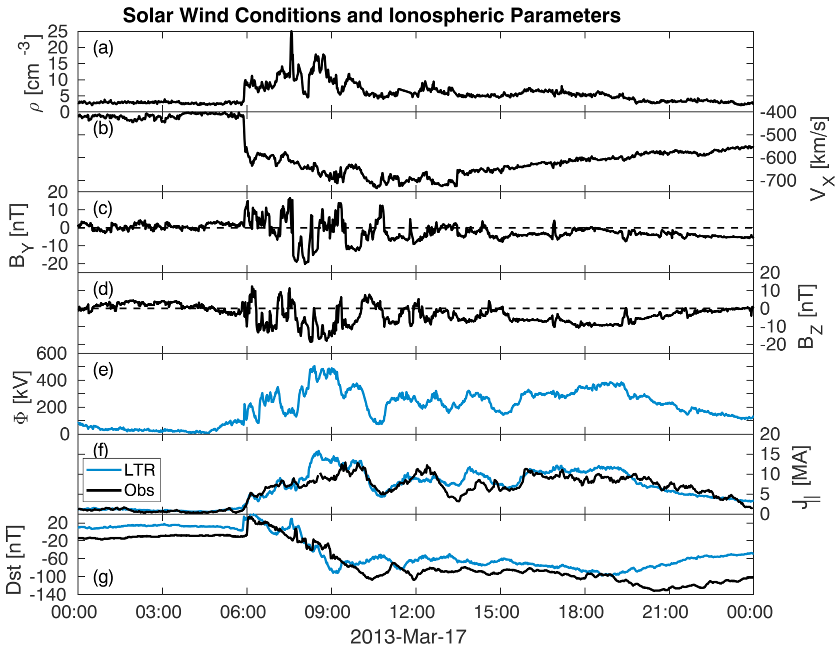

Figure 2. Solar wind conditions from the OMNI database and ionospheric parameters from Lyon-Fedder-Mobarry-Thermosphere Ionosphere Electrodynamics General Circulation Model-Rice Convection Model (LTR) simulation results and observations for 17 March 2013. (a) Solar wind density. (b) Solar wind velocity V_X. (c and d) IMF B_Y and B_Z in geocentric solar magnetospheric. (e) Simulation results of cross polar cap potential. (f) Total field-aligned current that flows into the ionosphere obtained from the model output (blue) and Active Magnetosphere and Planetary Electrodynamics Response Experiment data (black). (g) Dst index obtained from model output (blue) and CDAWeb database (black). The time on the horizontal axis is universal time.

3. SAPS Simulation Results

3.1. SAPS Identification and Comparison with DMSP Observations

Figure 3 shows the SAPS identified in the simulation results and comparison with those observed by the DMSP F18 satellite during three 10-min intervals: 10:12–10:22, 11:53–12:03, and 15:17–15:27 UT. The DMSP F18 measurements are shown in black. Figures 3a–3c show electron precipitation energy flux (EnFlux). The simulated precipitation energy fluxes are shown in blue, which are sampled from the MIX outputs along the trajectory of the DMSP satellite. Note the DMSP satellite was flying poleward during the three intervals shown here. The EnFlux profiles are shown to represent the auroral region. The equatorward boundary of auroral electron precipitation is indicated by the vertical dashed lines, which is determined where the EnFlux drops to 10% of the peak value. Figures 3d–3f show the westward ion drift (WID) velocity from the DMSP measurements and simulation results. It can be seen from the black curves that before the F18 satellite entered the aurora zone, additional westward ion flow channels were detected in the subauroral area. The ion drift velocities sampled in the simulation results are plotted in blue, which also show a substantial flow channel at somewhat lower latitudes than the equatorward boundary of auroral electron precipitation. These subauroral westward convections are interpreted as the definitive feature of SAPS (Foster & Burke, 2002; Koustov et al., 2008). It should be pointed out that while the simulation results do not always show an unambiguous secondary peak of WID, the drift velocity profiles do level off before dropping, which imply the existence of a separate subauroral convection flow channel. The peaks of SAPS flow channels in the simulation results are indicated by the red crosses in Figures 3d–3f. It is also noteworthy that the auroral region and SAPS channels are detected at somewhat later times in the simulation results compared to those in the DMSP F18 data, which imply that the auroral boundary is at a higher latitude in the model. Figures 3g–3i show the ionospheric FACs derived from the DMSP measurements of simulation results. The DMSP observed FAC was derived from the Special Sensor Magnetometer (SSM) magnetometer measurements of magnetic perturbations based on the Active Magnetosphere and Planetary Electrodynamics Response Experiment's law. The simulated FAC is output from the MIX module. It can be seen that the SAPS region in both DMSP observations and LTR simulations are collocated with the positive FACs. Note here both observed and simulated FACs are positive when flowing into the ionosphere and that the DMSP

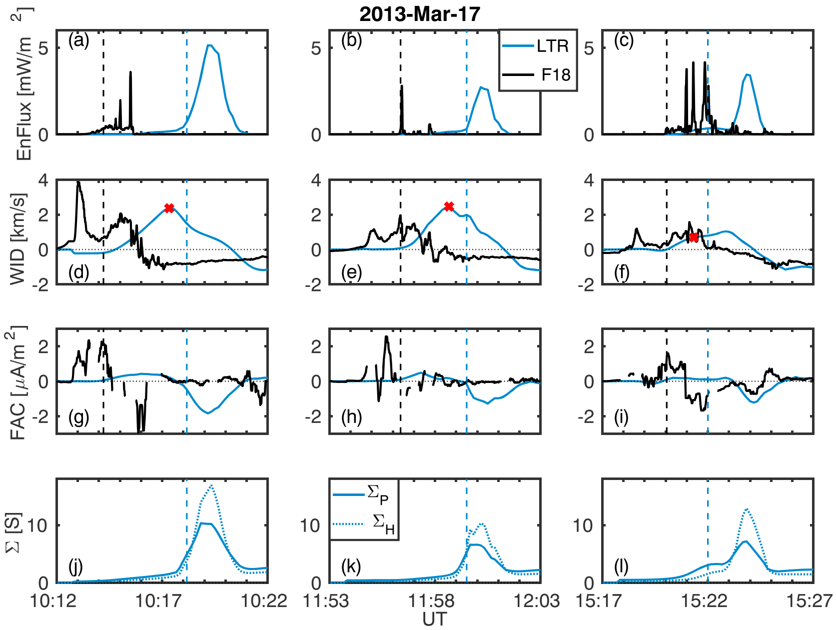

Figure 3. Comparison of Defense Meteorological Satellite Program (DMSP) F18 measurements and the Lyon-Fedder-Mobarry-Thermosphere Ionosphere Electrodynamics General Circulation Model-Rice Convection Model (LTR) simulation results of electron precipitation energy flux, westward ion drifts (WID), field-aligned current (FAC), and Pedersen/Hall conductances during three DMSP F18 crossings of the auroral zone: (left) 10:12–10:22 UT, (center) 11:53–12:03 UT, (right) 15:17–15:27 UT. (a–c) Precipitating electron energy flux (EnFlux) measured by the DMSP F18 SSJ (black) and sampled from the LTR simulation results (blue). (d–f) WID from DMSP measurements (black) and LTR simulations (blue). (g–i) FAC derived from DMSP/SSM magnetometer measurements of magnetic perturbations (black) and LTR simulations (blue). (j–l) LTR simulation results of ionospheric Pedersen (solid blue) and Hall (dotted blue) conductances. The simulated electron energy flux, WID, and FAC shown here are sampled from the Magnetosphere-Ionosphere Coupler/Solver outputs along the trajectories of the DMSP F18 satellite during the crossings. The simulated ionospheric conductances are height-integrated conductivities of the Thermosphere Ionosphere Electrodynamics General Circulation Model outputs. The observed FACs are derived from the magnetic perturbations measured by the SSM magnetometer onboard the DMSP F18 satellite. The vertical dashed lines correspond to where the EnFlux drops to 10% of the peak value during each interval, which are used to indicate the equatorward boundary of auroral electron precipitation. The red crosses in (d)–(f) indicate the peaks of subauroral WID. The DMSP F18 is flying poleward during these intervals.

trajectories during the three intervals shown here are on the duskside. It implies that the SAPS is collocated with the Region 2 FAC. Figure 3 (j-l) shows the ionospheric Pedersen and Hall conductance with solid and dotted curves, respectively. Here the conductances are both derived from the TIEGCM outputs of Pedersen and Hall conductivities by integrating along the altitude. It can be seen that the SAPS region corresponds to much lower ionospheric conductance than that in the auroral region.

In order to further illustrate the SAPS structure, we show the ionospheric states at the times when SAPS peak velocities are detected by the virtual DMSP F18 satellite analyzed in Figure 3. Figure 4 shows the simulation results at 10:17:20, 11:58:40, and 15:21:20 UT in the left, center, and right column, respectively, which correspond to the times indicated by the red crosses in Figures 3d–3f. Figures 4a–4c show the plasma zonal drift velocity in the ionosphere with the black arrows. The drift velocity is calculated from $\vec{E} \times \vec{B}$, where $\vec{E}$ is derived from MIX outputs of the ionospheric electrostatic potential and $\vec{B}$ is assumed to be a dipole geomagnetic field. Note the MIX module assumes an ionospheric shell with a radius of 1.02 R_E. The altitude of ion flow channel here is roughly 128 km. The convection velocities are evaluated at 24 MLT hours and every 1° from 40° to 80° magnetic latitude. The scale length is shown on the top left of the middle panel for 2 km/s. The velocity vectors show the westward drift channel around 60° magnetic latitude on the duskside, which is below the equatorward boundary of the electron auroral precipitation. The DMSP trajectories during the three intervals in Figure 3 are shown with the thick black curves. The red crosses on the trajectories indicate the positions of the virtual satellite at the current time, namely, when the SAPS peak velocity is identified. Figures 4d–4f show the MIX outputs of EnFlux into the ionosphere using the same colorbar. The bright color represents the aurora region, which spans equatorward to about 65° magnetic latitude on the duskside

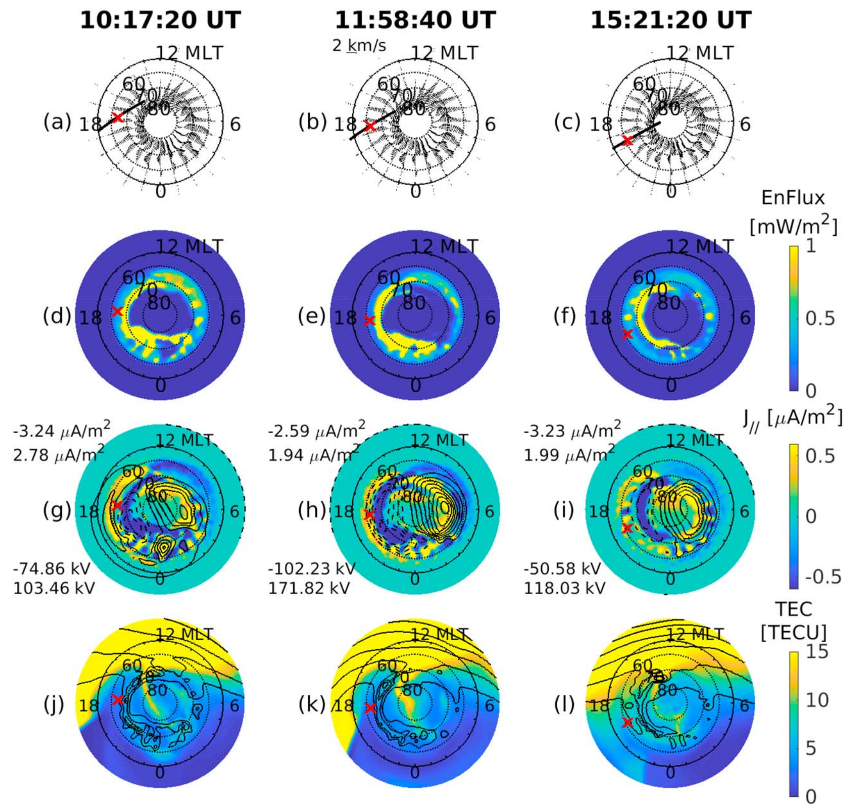

Figure 4. Simulation results of the ionospheric states at three universal times when subauroral polarization stream peak velocity is identified by the virtual Defense Meteorological Satellite Program (DMSP) F18 satellite. (a–c) Magnetosphere-Ionosphere Coupler/Solver (MIX) outputs of ion zonal drifts sampled at 24 bins from 0 to 23 magnetic local time (MLT), and from magnetic latitude of 40° to 80° in every 1°. The thick black curves show the trajectories of the virtual DMSP F18 during the 10-min intervals shown in Figure 3. The red crosses indicate the positions of the virtual satellite at the times shown here, which also correspond to the red crosses in Figure 3. (d–f) MIX outputs of electron precipitation energy flux into the ionosphere. (g–i) MIX outputs of field-aligned current density ($J_{//}$, background color) and electrostatic potential (ϕ, black contours) in the Northern Hemispheric ionosphere. Positive field-aligned current flows into the ionosphere. Positive potential is shown with the solid lines and negative with the dashed. The contours are leveled at multiples of 20 kV. The numbers on the left are the min and max of $J_{//}$ (top) and ϕ (bottom). (j–l) Thermosphere Ionosphere Electrodynamics General Circulation Model outputs of ionospheric total electron content (TEC; background color) and height-integrated Pedersen conductance (black contours). The contours are leveled at multiples of 3 S. The DMSP F18 is flying poleward during these intervals.

at 10:17:20 and 11:58:40 UT and extends poleward to about 70° at 15:21:20 UT. The two-dimensional plots of auroral electron precipitation and ionospheric convection provide a straightforward view of the subauroral flow channel, which spans from the duskside to the midnight. The magnetic latitude of the SAPS flow channel is from 65° to <60°, which is higher than that found in the observational data (Foster & Vo, 2002). This displacement likely results from the poleward shifted distribution of the upward Region 1 FAC in LFM simulations (Zhang et al., 2011).

Figures 4g–4i show the MIX outputs of ionospheric FAC density $J_{//}$ and electrostatic potential ϕ in the Northern Hemisphere. The FAC density is indicated by the same colorbar where positive stands for downward current flowing into the ionosphere. The electrostatic potential is shown with black contour lines, where solid lines stand for positive potential and dashed for negative. The contours are leveled at multiples of 20 kV. The FAC density range is shown in the top left, and the potential range is shown in the bottom left of each panel. The locations where SAPS peak is detected by the virtual satellite are shown by the red crosses. It can be seen that the electron auroral precipitation is collocated with the upward FAC on the duskside, which is associated with region 1, while SAPS are collocated with the downward FAC, which is associated with region 2 on the duskside.

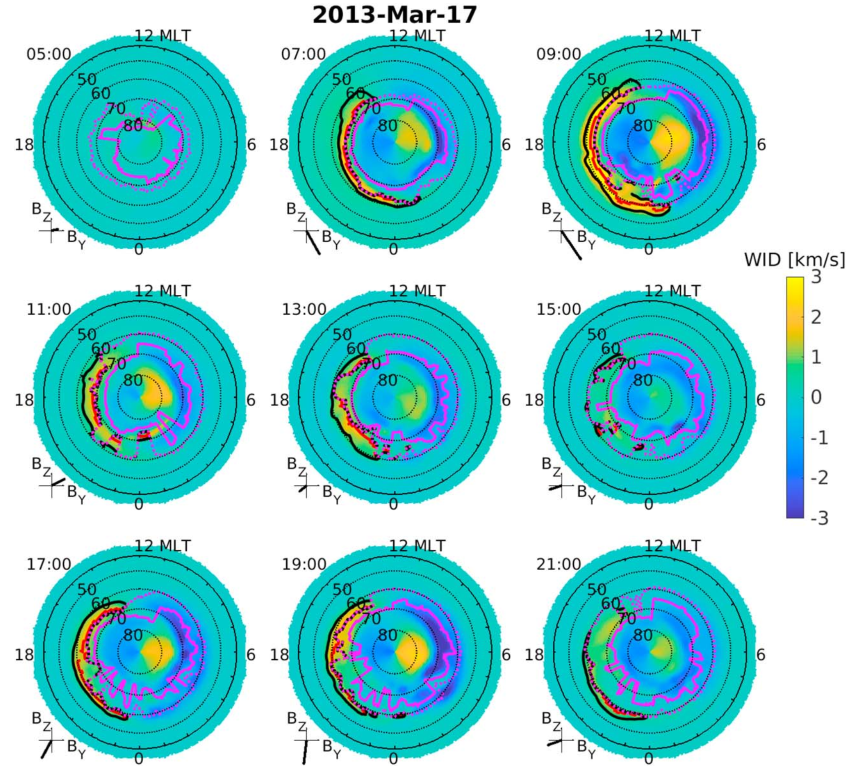

Figure 5. Distribution of ionospheric zonal drift velocity at nine universal times from 05:00 to 21:00 UT. Westward is positive. Auroral precipitation peaks at each magnetic local time (MLT) are indicated by the solid magenta lines. Equatorward boundaries of the electron precipitation oval are indicated by the dotted magenta lines. Subauroral polarization stream (SAPS) channels are indicated by the thick black lines. SAPS peaks are shown with the red lines. The global structure of SAPS channels can be told from the thick black lines.

Figures 4j–4l show the TIEGCM outputs of ionospheric TEC and height-integrated Pedersen conductance in the Northern Hemisphere. Note the colorbar is intentionally saturated to highlight the TEC variation on the duskside where SAPS peak velocities are identified. The TEC at the SAPS peak location is lower compared to that at the latitudes higher or lower than it. The trough-like structure appears to be consistent with the enhanced poleward electric field that drives the SAPS. The TEC plots also show a poleward extension in the dayside high latitude, which is identified as the tongue of ionization. The Pedersen conductance is derived from the TIEGCM outputs of Pedersen conductivity by integrating along the altitude. The contours are leveled at multiples of 3 S. The collocation between the SAPS and region 2 FAC as well as the low ionospheric TEC is in agreement with the statistical study based on DMSP data (He et al., 2018) and supports the mechanism that SAPSs are generated as region 2 FAC flows into the low conductance ionospheric region.

3.2. SAPS Global Structure

Having shown that the coupled LTR model can basically reproduce the definitive observational features and drivers of SAPS, we can characterize the global structure of SAPS with the simulation results. Figure 5 shows the global distribution of ion zonal drift velocity in the ionosphere from 05:00 to 21:00 UT at every 2 hr. Here the ion drift velocity is derived from the MIX outputs with the same method used for Figures 4a–4c. The positive velocity is westward. The SAPS region is quantitatively determined by comparing the electron auroral precipitation and ionospheric convection. We begin by identifying the equatorward boundary of the electron aurora oval with the MIX outputs of EnFlux. At each MLT, the latitudinal peak of EnFlux is first found. The electron precipitation peaks of all MLTs are shown by the solid magenta curves. The electron auroral equatorward boundary at each MLT is then determined as the latitude at which the EnFlux drops to 10% of the precipitation peak of that MLT. The electron auroral equatorward boundary is shown with the dotted magenta curve. SAPS are identified at each MLT bin being considered if there is a substantial WID, namely, greater than 500 m/s (Foster & Vo, 2002), found below the latitude of the electron auroral equatorward boundary. The SAPSs are marked with two thick black curves, which delimit the full width half maximum of the SAPS convection channel in the subauroral region. Within the SAPS channel, the latitude Λ at which the latitudinal peak velocity V_S is identified is shown with the red curve. The IMF B_Y and B_Z in geocentric solar magnetospheric are shown at the bottom left of each panel in Figure 5. The B_Y and B_Z axes range from −5 to 5 nT. The IMF is obtained from the OMNI database with 20-min shift in time, which is roughly the reconfiguration time required for the ionospheric convection to establish (Clauer & Friis-Christensen, 1988).

At 05:00 UT before the storm started, the IMF was weakly northward, and there is hardly any SAPS detected. The IMF turned strongly southward about 1 hr after the storm onset at 07:00 UT. A SAPS channel was detected in the duskside subauroral region, which spans from early afternoon to postmidnight. It is observed that the latitude of the SAPS decreases with MLT. The latitudinal width of the SAPS also decreases with MLT, forming the so-called wedge-shape structure. The spatial distribution of SAPS is consistent with the statistically average features (Foster & Vo, 2002) and the recently reported observation of SAPS in the main phase (He et al., 2018). By 09:00 UT when the IMF B_Z was even stronger southward, the SAPS has broadened both longitudinally and latitudinally with an overall equatorward expansion. The magnitude of SAPS velocity is also enhanced compared to 07:00 UT. In the next a few hours till 15:00 UT, the IMF is not as strongly southward and the SAPS channel shrunk to a narrower MLT ranging from pre-dusk to pre-midnight. The SAPS channel also became longitudinally discontinuous when the driving condition is weaker. From 17:00 to 19:00 UT, another period of southward IMF was impacting the Earth. The SAPS channel expands to below 60° magnetic latitude and approaches postnoon. The solar wind and IMF conditions returned to typical values of quiet time by 21:00 UT, when SAPS were weak and mostly localized between dusk and midnight.

3.3. SAPS Dynamic Evolution

With the SAPS global structures quantitatively characterized at different times as shown in Figure 5, we now further explore the dynamic evolution of SAPS by examining the dependence of SAPS parameters on the IMF B_Z and storm activity level. SAPS are treated as a two-dimensional structure varying with MLT and magnetic latitude. We use the latitudinal peak of SAPS velocity (V_S) at each MLT to characterize the magnitude of SAPS. V_S at all MLT of the entire day is plotted in Figure 6 a. Note that the V_S distribution shows that SAPS are mostly detected from postnoon to postmidnight. Almost no SAPSs are identified between 02:00 and 05:00 UT when IMF B_Z was northward with small magnitudes. The mean value of V_S over all MLTs is shown in Figure 6b. The largest V_S occurred between ∼07:30 and 10:00 UT when IMF B_Z was southward with large magnitudes. SAPS location is characterized with the latitude Λ at which V_S is detected. The temporal variations of the MLT distribution of Λ and its longitudinal mean $\bar{\Lambda}$ are shown in Figures 6c and 6d. The latitudinal size of SAPS $\delta\Lambda$ is characterized with the full width half maximum of the latitudinal profile of SAPS velocity at each MLT. The $\delta\Lambda$ and $\overline{\delta\Lambda}$ are shown in Figures 6e and 6f. The Dst index and IMF B_Z are shown in Figures 6e and 6f, respectively.

SAPS signatures are detected after the beginning of the day, although the SAPS magnitude from 00:00 to 02:00 UT was only a few hundred meters per second. The SAPS were confined to a few MLT hours near dusk at ∼70° magnetic latitude. The SAPS latitudinal width is only 1–2°. These SAPS signatures are attributed to the southward IMF during the last universal time hour of 16 March 2013. They then gradually shrink to high latitude and disappear over the period of northward IMF till 05:00 UT.

SAPS are detected again when the IMF turned southward even before the storm onset at 05:55 UT. The peak magnitude increases to more than 3 km/s by 09:00 UT during the main phase of the storm (Figure 6a). It can be seen from Figure 6b that SAPS initiate at ∼15 MLT before the storm onset with limited longitudinal coverage. But the strongest SAPS magnitude occurred a bit later than 18 MLT after the storm onset. There is a brief interruption of SAPS growth around 07:30 UT, which is attributed to the northward turning of IMF. SAPS magnitude is drastically strengthened at all duskside MLT from 07:30 to 10:30 UT. The mean latitude in Figure 6c shows that SAPS are overall expanding equatorward in the main phase. Figure 6d indicates that near the storm onset, SAPS latitude is decreasing with MLT from over 70° to ∼60°. The mean latitudinal width in Figure 6e shows that the SAPS channel is broadening during the main phase. Specifically, the latitudinal width is larger near noon and becomes narrower toward midnight, forming the so-called wedge shape, as shown in Figure 6e from 06:30 to 07:10 UT.

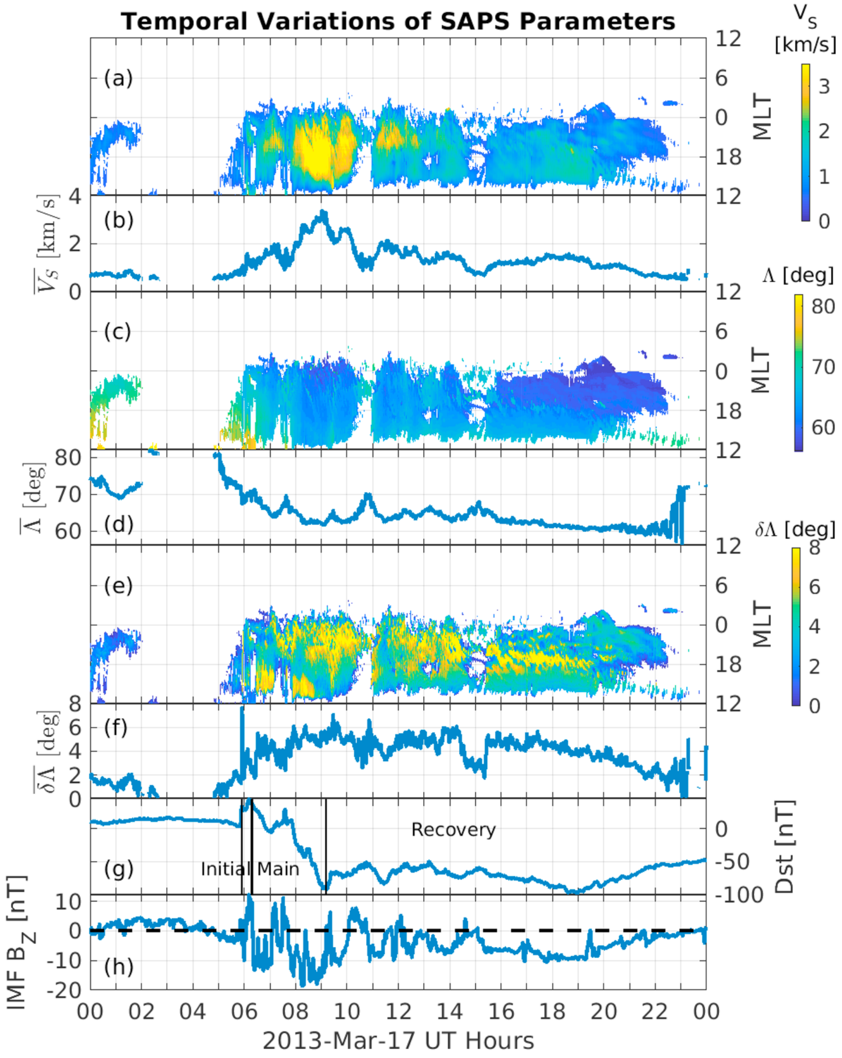

Figure 6. Temporal variations of subauroral polarization stream (SAPS; a) latitudinal peak drift velocity V_S at all magnetic local time (MLT); (b) longitudinal mean of V_S; (c) the latitude Λ at which V_S is detected; (d) longitudinal mean of Λ; (e) latitudinal width $\delta\Lambda$ at all MLT; (f) longitudinal mean of $\delta\Lambda$; (g) Dst index derived from model outputs; (h) IMF B_Z in geocentric solar magnetospheric.

In the recovery phase, the SAPS magnitude starts to gradually decrease after 09:00 UT. However, the mean latitude of SAPS stays around 60° magnetic latitude and the mean width maintains 4° to 6° for about 10 hr instead of recovering to prestorm values instantly. A rebound of the SAPS magnitude is seen from 09:30 to 10:00 UT, which is correlated with the southward turning of IMF following the brief northward period after 09:00 UT. It is interesting to note that an inverse wedge shape is formed from 08:40 to 09:20 UT and from 09:40 to 10:20 UT, when the SAPS channel is wider near midnight and narrower in the postnoon. The inverse wedge shape appears to be associated with the weakening of southward IMF. The SAPS magnitude resumes decreasing after 10:00 UT when the IMF becomes northward again. The dip around 15:00 UT in SAPS magnitude and width and poleward motion is also accompanied by the weakening of the southward IMF.

From 15:30 to 19:30 UT, the IMF is continuously southward. The overall magnitude of SAPS is below 2 km/s. The SAPS channel is widest near the dusk and is narrower toward the midnight and postnoon, forming a crescent shape distribution, as shown in Figure 5 bottom row. The SAPS magnitude and width decrease continuously after 19:00 UT when the Dst is also recovering with both the decreasing IMF B_Z magnitude and solar wind velocity. Besides the variations on the scale of hours, it is also visible that the SAPS magnitude and structure profiles show more fluctuating behaviors compared to that of IMF B_Z, which implies that the SAPS are very dynamic structures associated with the magnetosphere-ionosphere-thermosphere coupling.

Table 1
Correlation Coefficients Between SAPS Parameters and IMF B_Z and Dst index

	$\overline{V_S}$	$\bar{\Lambda}$	$\overline{\delta\Lambda}$
Dst	−0.34	0.77	−0.55
B_Z	−0.57	0.54	−0.47

Note. SAPS = subauroral polarization stream; IMF = interplanetary magnetic field.

4. Discussion and Future Work

In this study, the CMIT model with ring current extension is used to investigate the SAPS global structure and dynamic evolution during the 17 March 2013 storm event. SAPS not only involve processes in different geospace domains, including the magnetosphere, ring current, ionosphere, and thermosphere, but also require distinct characterizations of plasma, including MHD description and kinetic treatments of the ions and electrons. The LFM-TIEGCM-RCM represents a state-of-the-art integrated geospace model that can self-consistently model the magnetosphere, ring current, ionosphere and thermosphere, and the dynamic coupling between these regimes. The simulated total ionospheric FAC and Dst index are found to be very close to available observational data, indicating reasonably consistent system-level responses in the modeling results. The analysis of subauroral convection further shows good agreement with the DMSP F18 measurements, demonstrating that the coupled LTR model is able to capture the fundamental structure and generation physics of SAPS.

The SAPS magnitude and spatial coverage are quantitatively characterized and their dependence on IMF B_Z are analyzed. We found a persistent flow channel in the subauroral region which is identified as SAPS. By comparing with the ionospheric FAC density and TEC map, it is found that the SAPS channel is collocated with the region 2 FAC on the duskside and a trough-like structure in the TEC map. This correlation supports the driving mechanism proposed in Anderson et al. (1993) in which a fraction of the downward region 2 FAC flows into the low ionospheric conductance region at subauroral latitudes. A strong poleward electric field is thus required to maintain the current continuity that drives the enhanced WID. This scenario is also supported by recent multisatellite analysis of SAPS (He et al., 2018).

It should be pointed out that the SAPS found in the model are at a higher latitude compared to that observed by the DMSP satellite. This displacement is likely a result of ring current effects. Wiltberger et al. (2017) has shown that the dipole magnetic field used in LFM-RCM is relatively underinflated compared to the TS07d empirical magnetic field model (Tsyganenko & Sitnov, 2007). As a result, the inner magnetosphere pressure peak is more outward, thus yielding a more poleward region 2 FAC. The ionospheric outflow has also been found to play an important role in generating a more realistic magnetic field topology (Brambles et al., 2013). Therefore, incorporating an ionospheric outflow model, such as the Ionosphere/Polar Wind Model, into the LTR model for ionospheric outflow effects may produce a more reasonable distribution of inner magnetospheric pressure and more consistent SAPS locations with observations (Varney et al., 2015).

The SAPS channel is less separated from the auroral convection compared with that observed by the DMSP satellite. This may be because the auroral precipitation model being used lacks the diffuse aurora, which is the dominant provider of precipitation energy flux (Newell et al., 2009). Besides, soft electron precipitation has also been shown to have a significant influence on the ionospheric plasma state and thermospheric heating (e.g., Su et al., 1999). Efforts are ongoing to include the diffuse and soft precipitation and ion precipitation into the model.

The global structure of SAPS can be quantitatively determined with the model results. The SAPS wedge-shaped flow channel is observed in the beginning of the main phase (Figure 5, top middle panel). An inverse wedge shape is also seen when the southward IMF is weakening (Figure 5, top right panel). The SAPS flow channel shows crescent distribution in the late recovery phase. The westward drift flow sometimes becomes discontinuous in the recovery phase. The large variations with longitude, latitude, and in magnitude suggest that SAPS are very dynamic structures and are strongly responsive to the southward IMF. The rapid evolution of SAPS may be attributed to the auroral streamers, which can enhance the ring current pressure (Gallardo-Lacourt et al., 2017). The correlation coefficients between the averaged SAPS parameters and IMF B_Z and the Dst index are shown in Table 1, which represent the statistical connections between the SAPS phenomena and the IMF driving and the geomagnetic activity level. Here B_Z is shifted by 20 min for correlation analysis. While the SAPS structure has been shown to be qualitatively consistent with southward IMF, the quantitative correlation coefficients are generally below 0.8, which could be due to the rapid oscillations of SAPS structure parameters. The connections between SAPS evolution and southward IMF in this event simulation are consistent with the statistical results of He et al. (2017). It is inferred that the enhancement of ring current during southward IMF contributes to the strengthening of region 2 FAC that flows into the subauroral region and facilitates the growth of SAPS.

In this study, SAPS during the 2013 St. Patrick's Day storm are investigated with the coupled magnetosphere-ring current-ionosphere-thermosphere model. The key features of SAPS and their driving processes are captured by the model and show good consistency with observational data. SAPS are collocated with the region 2 FAC on the duskside and TEC trough in the ionosphere. The region 2 FAC flowing into the low conductance region in the subauroral latitude results in the strong poleward electric field that drives the enhanced SAPS flow. The global structure and evolution of SAPS are quantitatively characterized using the modeling results. SAPS evolution involves latitudinal, longitudinal, structure, and drift velocity variations. SAPS structure is found to be very dynamic and sensitive to IMF B_Z. The SAPS magnitude, location, and latitudinal width are correlated with the strength of the southward IMF. It is suggested that SAPS evolution is closely related to the storm activity. This is the first time that the high-resolution LFM, TIEGCM, and RCM models are coupled together, which is necessary to explore the mesoscale processes like SAPS. To better understand the coupling mechanism of SAPS, we will in the future work look at the SAPS influences on the ionosphere-thermosphere and how the subauroral dynamics feedback to the inner magnetosphere. Improved models of ring current and precipitation are required.

Acknowledgments
This work is funded by NASA MAG16_2-0050 and the Visitor Program of High Altitude Observatory of National Center for Atmospheric Research. This work is also supported by NASA Grants 80NSSC17K0013, NNX17AI42G, NNX15AB83G, and NNX14AE06G. The National Center for Atmospheric Research is sponsored by the National Science Foundation. We acknowledge use of NASA/GSFC's Space Physics Data Facility's CDAWeb service and OMNI data. We thank the AMPERE team and the AMPERE Science Center for providing the Iridium-derived data products. We thank NOAA/NESDIS/National Geophysical Data Center for the provision of the DMSP data. We thank the Kyoto, Japan, World Data Center for providing the Dst index. We acknowledge high-performance computing support from Cheyenne (doi:10.5065/D6RX99HX) provided by NCAR's Computational and Information Systems Laboratory, sponsored by the National Science Foundation. Dong Lin would like to thank Michael Wiltberger for his help with testing the coupled model and thank William Lotko for his help with revising the manuscript. The model outputs that are used in this paper are being preserved in the NCAR DASH repository and can be accessed publicly at their website (https://doi.org/10.26024/q3vy-ad49).

References

Anderson, P., Carpenter, D., Tsuruda, K., Mukai, T., & Rich, F. (2001). Multisatellite observations of rapid subauroral ion drifts (SAID). *Journal of Geophysical Research*, *106*(A12), 29,585–29,599. https://doi.org/10.1029/2001JA000128

Anderson, P., Hanson, W., Heelis, R., Craven, J., Baker, D., & Frank, L. (1993). A proposed production model of rapid subauroral ion drifts and their relationship to substorm evolution. *Journal of Geophysical Research*, *98*(A4), 6069–6078. https://doi.org/10.1029/92JA01975

Brambles, O., Lotko, W., Zhang, B., Ouellette, J., Lyon, J., & Wiltberger, M. (2013). The effects of ionospheric outflow on ICME and SIR driven sawtooth events. *Journal of Geophysical Research: Space Physics*, *118*, 6026–6041. https://doi.org/10.1002/jgra.50522

Califf, S., Li, X., Wolf, R., Zhao, H., Jaynes, A., Wilder, F., et al. (2016). Large-amplitude electric fields in the inner magnetosphere: Van Allen probes observations of subauroral polarization streams. *Journal of Geophysical Research: Space Physics*, *121*, 5294–5306. https://doi.org/10.1002/2015JA022252

Clauer, C. R., & Friis-Christensen, E. (1988). High-latitude dayside electric fields and currents during strong northward interplanetary magnetic field: Observations and model simulation. *Journal of Geophysical Research*, *93*, 2749–2757. https://doi.org/10.1029/JA093iA04p02749

Clausen, L., Baker, J., Ruohoniemi, J., Greenwald, R., Thomas, E., Shepherd, S., et al. (2012). Large-scale observations of a subauroral polarization stream by midlatitude SuperDARN radars: Instantaneous longitudinal velocity variations. *Journal of Geophysical Research*, *117*, A05306. https://doi.org/10.1029/2011JA017232

Ebihara, Y., Nishitani, N., Kikuchi, T., Ogawa, T., Hosokawa, K., Fok, M.-C., & Thomsen, M. (2009). Dynamical property of storm time subauroral rapid flows as a manifestation of complex structures of the plasma pressure in the inner magnetosphere. *Journal of Geophysical Research*, *114*, A01306. https://doi.org/10.1029/2008JA013614

Fedder, J. A., Slinker, S. P., Lyon, J. G., & Elphinstone, R. (1995). Global numerical simulation of the growth phase and the expansion onset for a substorm observed by Viking. *Journal of Geophysical Research*, *100*(A10), 19,083–19,093. https://doi.org/10.1029/95JA01524

Foster, J., & Burke, W. (2002). SAPS: A new categorization for sub-auroral electric fields. *Eos, Transactions American Geophysical Union*, *83*(36), 393–394. https://doi.org/10.1029/2002EO000289

Foster, J., Erickson, P., Coster, A., Goldstein, J., & Rich, F. (2002). Ionospheric signatures of plasmaspheric tails. *Geophysical Research Letters*, *29*(13), 1623. https://doi.org/10.1029/2002GL015067

Foster, J., Erickson, P., Coster, A., Thaller, S., Tao, J., Wygant, J., & Bonnell, J. (2014). Storm time observations of plasmasphere erosion flux in the magnetosphere and ionosphere. *Geophysical Research Letters*, *41*, 762–768. https://doi.org/10.1002/2013GL059124

Foster, J., & Rideout, W. (2005). Midlatitude TEC enhancements during the October 2003 superstorm. *Geophysical Research Letters*, *32*, L12S04. https://doi.org/10.1029/2004GL021719

Foster, J., Rideout, W., Sandel, B., Forrester, W., & Rich, F. (2007). On the relationship of SAPS to storm-enhanced density. *Journal of Atmospheric and Solar-Terrestrial Physics*, *69*(3), 303–313. https://doi.org/10.1016/j.jastp.2006.07.021

Foster, J., & Vo, H. (2002). Average characteristics and activity dependence of the subauroral polarization stream. *Journal of Geophysical Research*, *107*(A12), 1475. https://doi.org/10.1029/2002JA009409

Gallardo-Lacourt, B., Nishimura, Y., Lyons, L., Mishin, E., Ruohoniemi, J., Donovan, E., et al. (2017). Influence of auroral streamers on rapid evolution of ionospheric SAPS flows. *Journal of Geophysical Research: Space Physics*, *122*, 12,406–12,420. https://doi.org/10.1002/2017JA024198

Galperin, Y. I., Ponomarev, V. N., & Zosimova, A. (1974). Plasma convection in polar ionosphere (*Tech Rep.*) Moscow: Institut Kosmicheskikh Issledovanii.

Garner, T., Wolf, R., Spiro, R., Burke, W., Fejer, B. G., Sazykin, S., et al. (2004). Magnetospheric electric fields and plasma sheet injection to low L-shells during the 4–5 June 1991 magnetic storm: Comparison between the rice convection model and observations. *Journal of Geophysical Research*, *109*, A02214. https://doi.org/10.1029/2003JA010208

Goldstein, J., Burch, J., & Sandel, B. (2005). Magnetospheric model of subauroral polarization stream. *Journal of Geophysical Research*, *110*, A09222. https://doi.org/10.1029/2005JA011135

He, F., Zhang, X.-X., & Chen, B. (2014). Solar cycle, seasonal, and diurnal variations of subauroral ion drifts: Statistical results. *Journal of Geophysical Research: Space Physics*, *119*, 5076–5086. https://doi.org/10.1002/2014JA019807

He, F., Zhang, X.-X., Wang, W., & Chen, B. (2016). Double-peak subauroral ion drifts (DSAIDS). *Geophysical Research Letters*, *43*, 5554–5562. https://doi.org/10.1002/2016GL069133

He, F., Zhang, X.-X., Wang, W., Liu, L., Ren, Z.-P., Yue, X., et al. (2018). Large-scale structure of subauroral polarization streams during the main phase of a severe geomagnetic storm. *Journal of Geophysical Research: Space Physics*, *123*, 2964–2973. https://doi.org/10.1002/2018JA025234

He, F., Zhang, X.-X., Wang, W., & Wan, W. (2017). Different evolution patterns of subauroral polarization streams (SAPS) during intense storms and quiet time substorms. *Geophysical Research Letters*, *44*, 10,796–10,804. https://doi.org/10.1002/2017GL075449

Huang, C.-S., & Foster, J. C. (2007). Correlation of the subauroral polarization streams (SAPS) with the Dst index during severe magnetic storms. *Journal of Geophysical Research*, *112*, A11302. https://doi.org/10.1029/2007JA012584

Koustov, A., Nishitani, N., Ebihara, Y., Kikuchi, T., Hairston, M., & Andre, D. (2008). Subauroral polarization streams: Observations with the Hokkaido and King Salmon SuperDARN radars and modeling. *Annales Geophysicae*, *26*(11), 3317–3327. https://doi.org/10.5194/angeo-26-3317-2008

Kunduri, B., Baker, J., Ruohoniemi, J., Thomas, E., Shepherd, S., & Sterne, K. (2017). Statistical characterization of the large-scale structure of the subauroral polarization stream. *Journal of Geophysical Research: Space Physics*, *122*, 6035–6048. https://doi.org/10.1002/2017JA024131

Lejosne, S., Kunduri, B., Mozer, F., & Turner, D. (2018). Energetic electron injections deep into the inner magnetosphere: A result of the subauroral polarization stream (SAPS) potential drop. *Geophysical Research Letters*, *45*, 3811–3819. https://doi.org/10.1029/2018GL077969

Lyon, J., Fedder, J., & Mobarry, C. (2004). The Lyon–Fedder–Mobarry (LFM) global MHD magnetospheric simulation code. *Journal of Atmospheric and Solar-Terrestrial Physics*, *66*(15-16), 1333–1350. https://doi.org/10.1016/j.jastp.2004.03.020

Lyons, L., Nishimura, Y., Gallardo-Lacourt, B., Nicolls, M., Chen, S., Hampton, D., et al. (2015). Azimuthal flow bursts in the inner plasma sheet and possible connection with SAPS and plasma sheet earthward flow bursts. *Journal of Geophysical Research: Space Physics*, *120*, 5009–5021. https://doi.org/10.1002/2015JA021023

Makarevich, R., & Dyson, P. (2008). Dual HF radar study of the subauroral polarization stream. *Annales Geophysicae*, *25*, 2579–2591.

Merkin, V., & Lyon, J. (2010). Effects of the low-latitude ionospheric boundary condition on the global magnetosphere. *Journal of Geophysical Research*, *115*, A10202. https://doi.org/10.1029/2010JA015461

Mishin, E., Nishimura, Y., & Foster, J. (2017). SAPS/SAID revisited: A causal relation to the substorm current wedge. *Journal of Geophysical Research: Space Physics*, *122*, 8516–8535. https://doi.org/10.1002/2017JA024263

Newell, P., Sotirelis, T., & Wing, S. (2009). Diffuse, monoenergetic, and broadband aurora: The global precipitation budget. *Journal of Geophysical Research*, *114*, A09207. https://doi.org/10.1029/2009JA014326

Pembroke, A., Toffoletto, F., Sazykin, S., Wiltberger, M., Lyon, J., Merkin, V., & Schmitt, P. (2012). Initial results from a dynamic coupled magnetosphere-ionosphere-ring current model. *Journal of Geophysical Research*, *117*, A02211. https://doi.org/10.1029/2011JA016979

Raeder, J., Cramer, W. D., Jensen, J., Fuller-Rowell, T., Maruyama, N., Toffoletto, F., & Vo, H. (2016). Sub-auroral polarization streams: A complex interaction between the magnetosphere, ionosphere, and thermosphere. *Journal of Physics: Conference Series*, *767*, 012021. https://doi.org/10.1088/1742-6596/767/1/012021

Richmond, A., Ridley, E., & Roble, R. (1992). A Thermosphere/Ionosphere General Circulation Model with coupled electrodynamics. *Geophysical Research Letters*, *19*(6), 601–604. https://doi.org/10.1029/92GL00401

Roble, R., Ridley, E. C., Richmond, A., & Dickinson, R. (1988). A coupled Thermosphere/Ionosphere General Circulation Model. *Geophysical Research Letters*, *15*(12), 1325–1328. https://doi.org/10.1029/GL015i012p01325

Shinbori, A., Otsuka, Y., Tsugawa, T., Nishioka, M., Kumamoto, A., Tsuchiya, F., et al. (2018). Temporal and spatial variations of storm time midlatitude ionospheric trough based on global GNSS-TEC and ARASE satellite observations. *Geophysical Research Letters*, *45*, 7362–7370. https://doi.org/10.1029/2018GL078723

Spiro, R., Heelis, R., & Hanson, W. (1979). Rapid subauroral ion drifts observed by Atmosphere Explorer C. *Geophysical Research Letters*, *6*(8), 657–660. https://doi.org/10.1029/GL006i008p00657

Su, Y-J, Caton, R. G., Horwitz, J. L., & Richards, P. G. (1999). Systematic modeling of soft-electron precipitation effects on high-latitude F region and topside ionospheric upflows. *Journal of Geophysical Research*, *104*(A1), 153–163. https://doi.org/10.1029/1998JA900068

Toffoletto, F., Sazykin, S., Spiro, R., & Wolf, R. (2003). Inner magnetospheric modeling with the Rice Convection Model. *Space Science Reviews*, *107*(1-2), 175–196. https://doi.org/10.1023/A:1025532008047

Tsyganenko, N., & Sitnov, M. (2007). Magnetospheric configurations from a high-resolution data-based magnetic field model. *Journal of Geophysical Research*, *112*, A06225. https://doi.org/10.1029/2007JA012260

Varney, R., Wiltberger, M., & Lotko, W. (2015). Modeling the interaction between convection and nonthermal ion outflows. *Journal of Geophysical Research: Space Physics*, *120*, 2353–2362. https://doi.org/10.1002/2014JA020769

Wang, W., Talaat, E. R., Burns, A. G., Emery, B., Hsieh, S.-y., Lei, J., & Xu, J. (2012). Thermosphere and ionosphere response to subauroral polarization streams (SAPS): Model simulations. *Journal of Geophysical Research*, *117*, A07301. https://doi.org/10.1029/2012JA017656

Wang, W., Wiltberger, M., Burns, A., Solomon, S., Killeen, T., Maruyama, N., & Lyon, J. (2004). Initial results from the Coupled Magnetosphere–Ionosphere–Thermosphere model: Thermosphere–ionosphere responses. *Journal of Atmospheric and Solar-Terrestrial Physics*, *66*(15-16), 1425–1441. https://doi.org/10.1016/j.jastp.2004.04.008

Wiltberger, M., Merkin, V., Zhang, B., Toffoletto, F., Oppenheim, M., Wang, W., et al. (2017). Effects of electrojet turbulence on a magnetosphere-ionosphere simulation of a geomagnetic storm. *Journal of Geophysical Research: Space Physics*, *122*, 5008–5027. https://doi.org/10.1002/2016JA023700

Wiltberger, M., Wang, W., Burns, A., Solomon, S., Lyon, J., & Goodrich, C. (2004). Initial results from the Coupled Magnetosphere Ionosphere Thermosphere model: Magnetospheric and ionospheric responses. *Journal of Atmospheric and Solar-Terrestrial Physics*, *66*(15-16), 1411–1423. https://doi.org/10.1016/j.jastp.2004.03.026

Wiltberger, M., Weigel, R., Lotko, W., & Fedder, J. (2009). Modeling seasonal variations of auroral particle precipitation in a global-scale magnetosphere-ionosphere simulation. *Journal of Geophysical Research*, *114*, A01204. https://doi.org/10.1029/2008JA013108

Yeh, H.-C., Foster, J., Rich, F., & Swider, W. (1991). Storm time electric field penetration observed at mid-latitude. *Journal of Geophysical Research*, *96*(A4), 5707–5721. https://doi.org/10.1029/90JA02751

Yu, Y., Jordanova, V., Zou, S., Heelis, R., Ruohoniemi, M., & Wygant, J. (2015). Modeling subauroral polarization streams during the 17 March 2013 storm. *Journal of Geophysical Research: Space Physics*, *120*, 1738–1750. https://doi.org/10.1002/2014JA020371

Yuan, Z., Qiao, Z., Li, H., Huang, S., Wang, D., Yu, X., & Yu, T. (2017). Subauroral polarization stream on the outer boundary of the ring current during an energetic ion injection event. *Journal of Geophysical Research: Space Physics*, *122*, 4837–4845. https://doi.org/10.1002/2016JA023570

Yuan, Z., Xiong, Y., Qiao, Z., Li, H., Huang, S., Wang, D., et al. (2016). A subauroral polarization stream driven by field-aligned currents associated with precipitating energetic ions caused by EMIC waves: A case study. *Journal of Geophysical Research: Space Physics*, *121*, 1696–1705. https://doi.org/10.1002/2015JA021804

Zhang, S.-R., Erickson, P. J., Zhang, Y., Wang, W., Huang, C., Coster, A. J., et al. (2017). Observations of ion-neutral coupling associated with strong electrodynamic disturbances during the 2015 St. Patrick's Day storm. *Journal of Geophysical Research: Space Physics*, *122*, 1314–1337. https://doi.org/10.1002/2016JA023307

Zhang, B., Lotko, W., Wiltberger, M., Brambles, O., & Damiano, P. (2011). A statistical study of magnetosphere–ionosphere coupling in the Lyon–Fedder–Mobarry global MHD model. *Journal of Atmospheric and Solar-Terrestrial Physics*, *73*(5-6), 686–702. https://doi.org/10.1016/j.jastp.2010.09.027

Zheng, Y., Brandt, P. C., Lui, A. T., & Fok, M.-C. (2008). On ionospheric trough conductance and subauroral polarization streams: Simulation results. *Journal of Geophysical Research*, *113*, A04209. https://doi.org/10.1029/2007JA012532